Available online at www.sciencedirect.com
ScienceDirect
Combustion and Flame 153 (2008) 367–383
Combustion and Flame
www.elsevier.com/locate/combustflame

Effects of H_2 enrichment on the propagation characteristics of CH_4–air triple flames

Alejandro M. Briones [a], Suresh K. Aggarwal [a,*], Viswanath R. Katta [b]

[a] *Department of Mechanical and Industrial Engineering, University of Illinois at Chicago, Chicago, IL 60607, USA*
[b] *Innovative Scientific Solutions, Inc., 2766 Indian Ripple Road, Dayton, OH 45440, USA*

Received 12 March 2007; received in revised form 27 January 2008; accepted 22 February 2008

Available online 7 April 2008

Abstract

The effects of H_2 enrichment on the propagation of laminar CH_4–air triple flames in axisymmetric coflowing jets are numerically investigated. A comprehensive, time-dependent computational model, which employs a detailed description of chemistry and transport, is used to simulate the transient ignition and flame propagation phenomena. Flames are ignited in a jet-mixing layer far downstream of the burner. Following ignition, a well-defined triple flame is formed that propagates upstream along the stoichiometric mixture fraction line with a nearly constant displacement velocity. As the flame approaches the burner, it transitions to a double flame, and subsequently to a burner-stabilized nonpremixed flame. Predictions are validated using measurements of the displacement flame velocity. As the H_2 concentration in the fuel blend is increased, the displacement flame velocity and local triple flame speed increase progressively due to the enhanced chemical reactivity, diffusivity, and preferential diffusion caused by H_2 addition. In addition, the flammability limits associated with the triple flames are progressively extended with the increase in H_2 concentration. The flame structure and flame dynamics are also markedly modified by H_2 enrichment, which substantially increases the flame curvature and mixture fraction gradient, as well as the hydrodynamic and curvature-induced stretch near the triple point. For all the H_2-enriched methane–air flames investigated in this study, there is a negative correlation between flame speed and stretch, with the flame speed decreasing almost linearly with stretch, consistent with previous studies. The H_2 addition also modifies the flame sensitivity to stretch, as it decreases the Markstein number (Ma), implying an increased tendency toward diffusive–thermal instability (i.e. $\mathrm{Ma} \to 0$). These results are consistent with the previously reported experimental results for outwardly propagating spherical flames burning a mixture of natural gas and hydrogen.
© 2008 The Combustion Institute. Published by Elsevier Inc. All rights reserved.

Keywords: Hydrogen–methane blends; Propagating triple flames; Diffusive–thermal instability; Preferential diffusion; Stretch–flame speed interactions

1. Introduction

There is a worldwide interest in developing hydrogen-based combustion systems, due to growing environmental concerns and the deteriorating supply–demand scenario with regard to fossil fuels. Fossil fuels are nonrenewable and a major source of pollutants,

* Corresponding author. Fax: +1 312 413 0441.
E-mail address: ska@uic.edu (S.K. Aggarwal).

0010-2180/$ – see front matter © 2008 The Combustion Institute. Published by Elsevier Inc. All rights reserved.
doi:10.1016/j.combustflame.2008.02.005

including CO_2, NO_x, UHC, and soot. In contrast, hydrogen represents a potentially unlimited source of energy that is environmentally clean, with NO_x being the major undesirable pollutant. There are, however, significant difficulties associated with hydrogen storage due to its high flammability limits, low ignition energy, and low volumetric energy content. There are also many unresolved issues with regard to H_2 combustion, such as knock, detonation, preignition, and flashback. In this context, hydrogen–hydrocarbon fuel blends offer a very promising alternative, as they can synergistically resolve the storage and combustion problems associated with hydrogen and the emission problems associated with fossil fuel combustion. Consequently, there has been considerable interest in investigating the combustion and emission characteristics of hydrogen–hydrocarbon fuel blends.

Several studies have been reported on the performance and emission characteristics of internal combustion engines using hydrogen–fossil fuel blends. These include studies dealing with a diesel engine using a hydrogen–vegetable oil blend [1] and spark ignition engines using a hydrogen–gasoline blend [2,3], a hydrogen–natural gas blend [4–8], and a hydrogen–methanol blend [9]. Bauer and Forest [10] investigated the effect of hydrogen addition on the performance of methane-fueled vehicles. It was shown that the wide flammability limits of hydrogen makes it possible to run SI engines at lower equivalence ratios using a hydrogen–methane blend, which lowers cylinder temperature and thereby NO_x emission. Al-Baghdadi [11] also observed a significant reduction in NO_x production in spark ignition engines when a hydrogen–ethanol mixture was used instead of gasoline.

Flame studies using hydrogen–hydrocarbon fuel blends have also been reported. Choudhuri and Gollahali [12] performed an experimental–numerical investigation of hydrogen–natural gas jet diffusion flames and observed a reduction in the soot concentration and emission index of CO (EICO), but an increase in EINO with hydrogen addition. Rortveit et al. [13] reported an experimental–numerical study of NO_x emissions in counterflow methane–hydrogen nonpremixed flames. Naha et al. [14,15] studied the emission characteristics of hydrogen–methane and hydrogen–*n*-heptane fuel blends using a counterflow flame, and observed significant reduction in NO_x emission in hydrogen–*n*-heptane flames. Fotache et al. [16] investigated the ignition characteristics of hydrogen-enriched methane flames at various pressures and identified three ignition limits, namely (i) hydrogen-assisted ignition, (ii) transition, and (iii) hydrogen-dominated ignition. Huang et al. [17] measured the flame speeds for natural gas–hydrogen mixtures and observed that the increase in H_2 content increases the flame speed exponentially, while the Markstein length transitions from positive to negative, implying a tendency toward diffusive–thermal instability. Law et al. [18] examined the effect of adding propane to hydrogen at different pressures and observed that propane reduces the tendency toward diffusive–thermal instability, whereas a pressure increase promotes diffusive–thermal instability, causing flame front wrinkling and higher flame speeds. Schefer [19] investigated the stabilization of hydrogen-enriched methane–air swirl-stabilized premixed flames. It was shown that hydrogen addition reduces the lean stability limit, allowing stable burner operation at lower flame temperature that is in turn beneficial for achieving lower NO_x emission. Similarly, Hawkes and Chen [20] studied hydrogen-enriched lean premixed methane–air flames and reported that hydrogen addition increases flame resistance to quenching, but also increases the tendency toward diffusive–thermal instability. In addition, the NO emission was observed to increase, while the CO emission decreased with hydrogen addition.

Our literature review indicates that while many important combustion and emission characteristics of hydrogen–hydrocarbon fuel blends have been investigated, the flame propagation characteristics of such fuel blends have not been examined. A fundamental understanding of the flame propagation characteristics of various fuel blends is important for the design of future combustion devices, such as spark ignition engines and gas turbine combustors, burning fuel blends. These characteristics are also important for the design of flame arrestors, which require laminar flame speed data for different fuel blends over a wide range of conditions. For example, a Venturi flame arrestor employs a flow restriction to increase the local mixture velocity above the local triple flame speed in order to capture a propagating flame.

In this paper, we report a fundamental investigation on the propagation characteristics of H_2-enriched CH_4–air flames in a laminar nonpremixed jet. The major objective is to examine the effects of H_2 enrichment on the propagation characteristics of CH_4–air flames in nonuniform mixtures in which the flame is subjected to flow nonuniformity and mixture fraction gradients, as well as curvature-induced, hydrodynamic, and unsteady stretch effects. A propagating flame is established by igniting the fuel–air mixture in the far field of a jet issuing a H_2–CH_4 mixture in a coflowing air jet. The ignition event is simulated by providing a small high-temperature zone containing small amounts of H and OH radicals. This high-temperature zone generates an ignition kernel that propagates upstream and rapidly develops into a triple flame, which then propagates upstream to-

ward the burner rim. The effects of hydrogen enrichment on the propagation characteristics of this triple flame are investigated using a comprehensive computational model that includes detailed descriptions of transport and chemistry. The choice of this configuration is based on several considerations. First, this configuration is relevant to many combustion systems, including gas turbines and internal combustion engines [21]. Second, it is difficult to establish lifted H_2–air or CH_4–air flames in a jet configuration due to the high mass diffusivity of these fuels (Sc < 1) [22]. Third, the present configuration is well suited to examine the propagation characteristics of triple flames established using hydrogen–methane fuel blends and to characterize the effects of hydrogen on stretch–flame speed interactions. Finally, investigations of triple flame propagation in laminar jets provide fundamental information for the understanding and modeling of turbulent flames. For instance, the stabilization [23,24] and propagation [25,26] of turbulent flames often involve triple flames, which are subjected to a wide range of mixture fraction gradient, stretch, and partial premixing. Consequently, several previous studies have investigated the effects of jet velocity [22,26], coflow velocity [27], partial premixing [25,28,29], heat release [30], and dilution [28,29] on laminar flame stabilization and propagation. However, the flame propagation characteristics associated with fuel blends have not yet been investigated.

It is important to note that a similar configuration involving triple flames has been employed in previous studies. Ruetsch et al. [30] reported the first numerical investigation of triple flames and thus laid the foundation for such studies. They showed that heat release redirects the flow ahead of the triple flame, reducing the flow velocity along the stoichiometric mixture fraction line, which reaches a local minimum just ahead of the triple flame. For a lifted triple flame, this local minimum flow velocity was defined as the local (triple) flame speed (S_{tri}) [30,31] at the triple point, while the upstream flow velocity was defined as the far field or global flame speed (U_F) [30,31]. In addition, it was shown that the global flame speed increases with the decrease in mixture fraction gradient, and in the limit of small mixture fraction gradient, the U_F/S_{tri} ratio is proportional to the square root of the density ratio of unburnt to burnt mixtures ($\sqrt{(\rho_u/\rho_b)}$) across the flame. Qin et al. [25] and Ko and Chung [26] investigated the propagation of CH_4–air triple flames in laminar jets and observed that the instantaneous displacement flame velocity (V_f),[1] which is the flame velocity in laboratory coordinates, remains nearly constant during propagation, while the local triple flame speed (S_{tri}) decreases with flame stretch and mixture fraction gradient. In addition, the global flame speed (U_F) was found to be about twice the laminar stoichiometric unstretched flame speed (S_L^0), while it was observed to be considerably higher (3–6 times) in turbulent jets [32]. It is also interesting to note that in both laminar [25,26] and turbulent flows [32] it was observed that an increase in jet velocity decreases the displacement flame velocity but increases the local flame speed, and that the local flame speed decreases with axial position due to the increase in mixture fraction gradient and flame curvature. This further highlights the fact that investigations of laminar triple flames can provide insight into the stabilization and propagation of turbulent flames.

Im and Chen [33] investigated the propagation of H_2–air triple flames in a nonpremixed jet. Similarly to previous studies [30,34], the global flame speed was found to be proportional to the square root of the density ratio across the flame. Another important observation from this study was that for H_2–air mixtures, the flame is shifted toward the air side and becomes asymmetric with respect to the stoichiometric mixture fraction ($f_s = 0.0285$) line,[2] since f_s is much smaller than 0.5. Consequently, the triple point, located at the intersection of the stoichiometric mixture fraction line and the flame surface, does not coincide with the flame leading edge, which is located at the local minimum flame curvature. This shift between the triple point and the leading edge is important in the context of determining the triple flame speed, since the experimental studies have generally reported the flame speeds at the leading edge [35], while the numerical investigations have computed these speeds at the triple point [25,29,33]. While this shift is also ob-

[1] It is important to note the inconsistencies in the definitions of S_{tri}, U_F, and V_f used in the literature. For instance, S_{tri} is also referred as the edge speed in Ref. [31], as the local displacement speed in Ref. [33], and as the flame propagation speed in Ref. [25]. Similarly, U_F is also referred as the stabilization speed in Ref. [33] and as the relative propagation speed in Ref. [32]. In addition, V_f is referred as the flamefront propagation velocity in Ref. [25] and as the net flame velocity in Ref. [32]. Here, we define S_{tri} as the local triple flame speed, U_F as the global flame speed, and V_f as the displacement flame velocity. Note that we use the term "speed" when referring to flame properties (i.e., relative velocities with respect to the incoming jet flow velocity such as S_{tri} and U_F), whereas the term "velocity" is used for absolute velocities (i.e., measured from a fixed coordinate system such as V_f).

[2] Note that for $f_s = 0.5$ the flame will be symmetric with respect to the stoichiometric mixture fraction line, and the locations of the triple point and the flame leading edge will coincide.

served for hydrocarbon flames, it becomes more pronounced for hydrogen flames, and therefore relevant to fuel blends containing hydrogen.

The preceding discussion indicates that several previous studies have focused on the propagation of triple flames in the context of pure fuels. However, the flame propagation characteristics of fuel blends have not been examined as yet.

2. Computational model

The numerical model is based on the solution of the time-dependent governing equations for a two-dimensional unsteady reacting flow [36,37]. Using cylindrical coordinates (r, z), these equations can be written as

$$\frac{\partial(\rho\Phi)}{\partial t} + \frac{\partial(\rho v\Phi)}{\partial r} + \frac{\partial(\rho u\Phi)}{\partial z} = \frac{\partial}{\partial r}\left(\Gamma^{\Phi}\frac{\partial\Phi}{\partial r}\right) + \frac{\partial}{\partial z}\left(\Gamma^{\Phi}\frac{\partial\Phi}{\partial z}\right) - \frac{\rho v\Phi}{r} + \frac{\Gamma^{\Phi}}{r}\frac{\partial\Phi}{\partial r} + S^{\Phi}. \quad (1)$$

Here t denotes the time, ρ the density, and u and v the axial (z) and radial (r) velocity components, respectively. The general form of the equation represents conservation of mass, momentum, species, or energy conservation, depending on the variable used for Φ. The diffusive transport coefficient Γ^{Φ} and source terms S^{Φ} are described in Ref. [36]. Introducing the overall species conservation equation and the state equation completes the equation set. A sink term based on an optically thin gas assumption was included in the energy equation to account for thermal radiation from the flame [38] in the form $q_{\text{rad}} = -4\sigma K_p(T^4 - T_0^4)$ [39], where T denotes the local flame temperature, and K_p accounts for the absorption and emission from the participating gaseous species (CO_2, H_2O, CO, and CH_4) expressed as $K_p = P\sum_k X_i K_{p,i}$, where $K_{p,i}$ denotes the mean absorption coefficient of the kth species, σ is the Stefan–Boltzmann constant, and T_0 is the ambient temperature. The value of $K_{p,i}$ is obtained using a polynomial approximation to the experimental data provided in Ref. [39].

The thermodynamic and transport properties appearing in the governing equations are temperature- and species-dependent. The thermal conductivity and viscosity of the individual species were based on Chapman–Enskog collision theory, following which those of the mixture are determined using the Wilke semiempirical formulas [40]. Chapman–Enskog theory and the Lennard–Jones potentials were used to estimate the binary diffusion coefficient between each species and nitrogen. The methane–air chemistry is modeled using a detailed mechanism that considers 31 species and 346 elementary reactions [41]. The major species included in the mechanism are CH_4, O_2, CO_2, CO, CH_2O, H_2, H_2O, C_2H_2, C_2H_4, C_2H_6, CH_3OH, and N_2, while the radical species include CH_3, CH_2, CH, CHO, H, O, OH, HO_2, H_2O_2, C_2H, C_2H_3, C_2H_5, CHCO, C, CH_2(s), CH_2OH, CH_3O, CH_2CO, and HCCOH. The mechanism has been validated previously for the computation of premixed flame speeds and the detailed structure of premixed and nonpremixed flames [42–44].

The finite-difference forms of the momentum equations are obtained using the QUICKEST scheme [45], while those of the species and energy are obtained using a hybrid scheme of upwind and central differencing. The pressure field is calculated at every time step by solving all of the pressure Poisson equations simultaneously and using the LU (lower and upper diagonal) matrix-decomposition technique.

Fig. 1 illustrates the computational domain. It consists of 100 × 50 mm in the axial (z) and radial (r) directions, respectively, and is represented by a staggered, nonuniform grid system. The reported results are grid-independent, as discussed in the next section. The minimum grid spacing is 0.05 mm in both the r- and z-directions. It is important to note that we have examined the grid resolution issues in a previous study [29] and found that a minimum grid spacing of 0.05 is sufficient to resolve the H and CH radical layers. An isothermal insert (2 × 0.8 mm) simulates the inner burner wall. The temperature at the burner wall was set at 300 K. The inner and outer jets are set with constant and uniform velocities of 10 and 30 cm/s, respectively. The inner jet issues a H_2–CH_4 mixture, while the outer jet issues air. A propagating flame is established by igniting the fuel–air mixing layer in the far field (35 mm above the burner rim). The ignition event is simulated by providing a small high-temperature zone with a temperature of 2000 K and a rectangular cross-sectional area of 2 mm^2, and containing small amounts of H and OH radicals. This high-temperature zone generates an ignition kernel that propagates upstream and rapidly develops into a triple flame, which then propagates upstream toward the burner rim and eventually stabilizes at the rim. A detailed numerical algorithm is developed to determine the propagation characteristics of this flame, which include the instantaneous displacement flame velocity and propagation speeds (i.e., local and global flame speeds), flame structure and dynamics near the triple point, and flame stretch–speed interactions for various levels of H_2 enrichment.

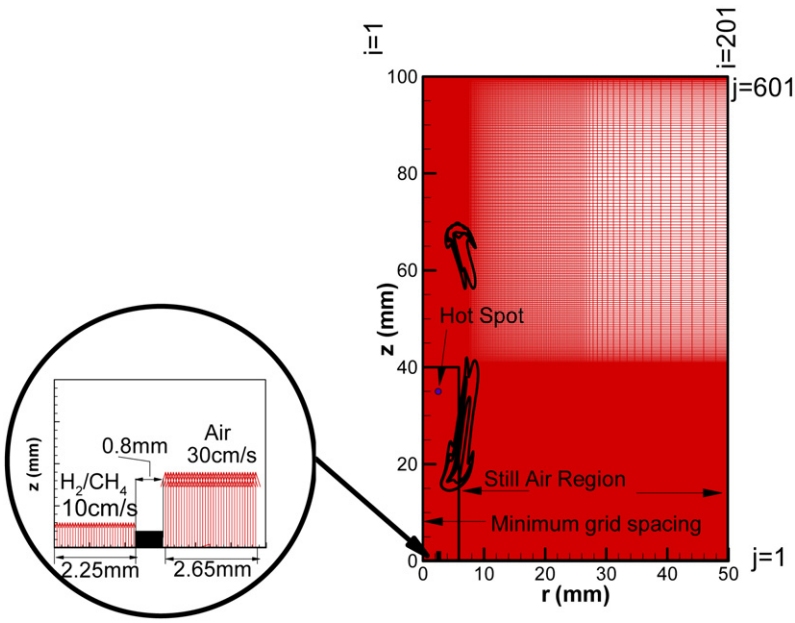

Fig. 1. Schematic of the computational grid used in the simulations. The small rectangle shows the minimum grid spacing region where the propagation flame front is located. A schematic of the computational domain is also shown.

3. Results and discussion

3.1. Validation of numerical model

The algorithm used for the simulation of propagating flames has been extensively validated in previous studies, using experimental data from burner-stabilized flames [36,46], lifted partially premixed flames [37], and propagating partially premixed flames [25]. The validation has included the comparison of the predicted and measured flame topology, liftoff heights (L_f), temperature, velocity and concentration fields, and instantaneous displacement flame velocity (V_f). In the following section, we will provide an additional validation by comparing the predicted and measured [47] displacement flame velocity (V_f) of a propagating CH_4–air triple flame.

3.2. Ignition and flame propagation

Fig. 2 presents the simulated results of transient ignition, flame propagation, and flame attachment for a propagating CH_4–air triple flame in terms of heat release rate contours. The first image at $t = 0$ ms corresponds to an instant when the high-temperature ignition source is removed, while the subsequent images show the formation and propagation of a triple flame. Following ignition, two reacting volumes (or kernels) are formed, as indicated by the image at $t = 3$ ms. One propagates downstream and is quickly extinguished. The other propagates upstream toward the burner and develops into a triple flame, which is the focus of this investigation. The triple flame structure develops at $t \sim 18$ ms. The flame propagates in a quasi-steady manner, i.e., at near-constant displacement flame velocity (V_f), from $z = 25$ mm to $z = 4$ mm, exhibiting a well-defined triple flame structure, as indicated in the snapshot at 48 ms. The three reaction zones, namely the rich premixed zone (RPZ), the lean premixed zone (LPZ), and the nonpremixed zone (NPZ), can be readily identified in the 18- and 48-ms images. As the flame approaches the burner rim (i.e., $z \approx 4$ mm), the length of the RPZ decreases, and the flame transitions to a double flame; i.e., the LPZ extinguishes. The flame reaches the burner rim at 88 ms, and during its stabilization at the rim, the RPZ extinguishes and the flame transitions from a double flame to a steady nonpremixed flame.

In Fig. 3, we present the temporal variation of axial flame position with respect to the burner rim ($d_f = z - 2$ mm) for the propagating 0%H_2-, 25%H_2-, 50%H_2-, and 75%H_2-enriched CH_4–air triple flames. As the amount of H_2 in the fuel blend is increased, the displacement flame velocity increases, as expected, and the time taken for the flame to reach the burner rim decreases considerably. In addition, the simulations indicate that for all four flames depicted in Fig. 3, the axial flame position (d_f) varies almost linearly with time. This behavior is consistent with the measurements reported by Ko and Chung [26], who showed that the flame position of propagating lami-

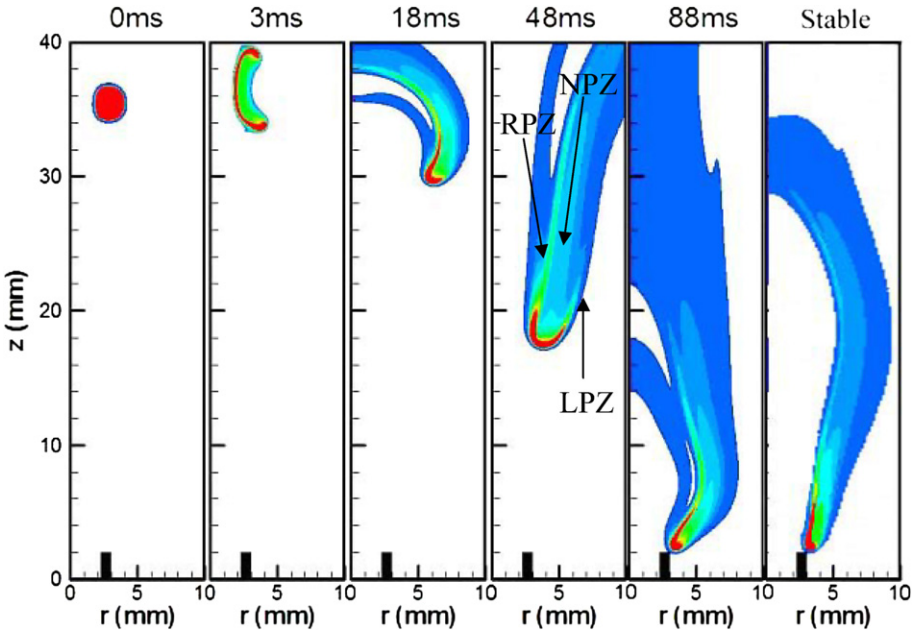

Fig. 2. Simulations showing the temporal evolution of ignition and flame propagation in terms of heat release rate contours for the pure CH_4–air flame. The three reaction zones, i.e., the rich premixed (RPZ), nonpremixed (NPZ), and lean premixed (LPZ) zones, are indicated in the snapshot at $t = 48$ ms.

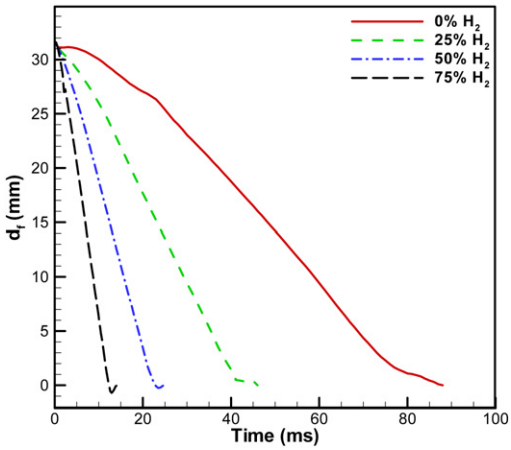

Fig. 3. Axial flame position (d_f) as a function of time for the 0%, 25%, 50%, and 75% H_2-enriched CH_4–air propagating flames.

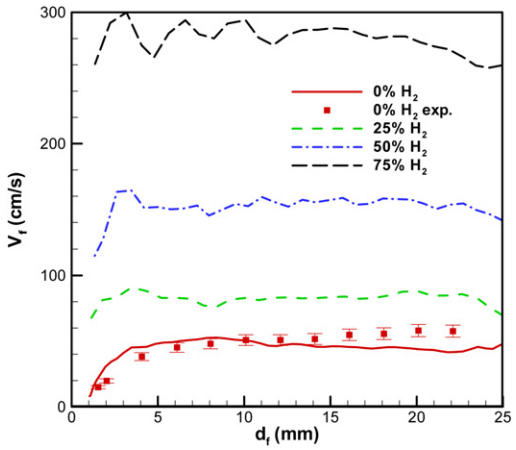

Fig. 4. Predicted displacement flame velocity (V_f) as a function of axial distance from the burner rim (d_f) for the 0%, 25%, 50%, and 75% H_2-enriched CH_4–air propagating flames. The measured V_f for a CH_4–air propagating flames from Ref. [47] is also shown for validation of the numerical model.

nar CH_4–air triple flames in nonpremixed jets varies linearly with time regardless of the jet inlet velocity.

Fig. 4 presents the instantaneous displacement flame velocity (V_f) as a function of flame position (d_f) for the four H_2-enriched CH_4–air flames discussed in the context of Fig. 3. The displacement flame velocity is obtained by calculating the rate of change of axial position of the triple point with time (i.e., $V_f = (\Delta z)_{tri}/\Delta t$). Note here that based on our simulations the radial component of the displacement flame velocity is negligible (i.e., $V_f = V_{f,z}$). The flame surface, which is needed for determining the triple point, is chosen to be the isocontour of the 0.0727 H_2O mass fraction, following Won et al. [35]. The measured displacement flame velocity as a function of flame position for a propagating CH_4–air triple flame, taken from Ref. [47], is also shown in the figure. There is

good agreement between the predicted and measured values. Both predictions and measurements indicate that V_f is nearly independent of time. Our predictions are also consistent with the measurements of Ko and Chung [26] for propagating CH_4–air triple flames with different jet inlet velocities. The displacement flame velocity decreases as the flame gets close to the burner rim ($d_f \sim 2$–3 mm) and tends to zero as the flame stabilizes at the rim. In addition, results in Fig. 4 indicate that as the amount of H_2 in the fuel blend is increased, V_f progressively increases, and the flame reaches the burner rim in a shorter time (cf. Fig. 3). The increase in V_f is due to an increase in the local triple flame speed, S_{tri} (discussed later), which in turn is due to the enhanced chemical reactivity, diffusivity, and preferential diffusion effects caused by H_2 enrichment. The aspects dealing with the effects of H_2 enrichment on the flame propagation characteristics, including stretch–flame speed interactions, are discussed in Section 3.4.

3.3. Flame base structure

In order to spatially resolve the various reaction zones of the propagating flame more clearly, we have previously developed a modified flame index [28,29], defined as

$$\xi_M = \left(\frac{f - f_S}{|f - f_S|}\right) \cdot \frac{1}{2}\left(1 + \frac{G_{FO}}{|G_{FO}|}\right). \tag{2}$$

Here the mixture fraction (f) is defined following Bilger [31], and G_{FO} is the flame index proposed by Takeno and co-workers [48]. Note that G_{FO} can only distinguish between premixed and nonpremixed reaction zones, while with the modified definition (i.e., Eq. (2)), $\xi_M = 1$ represents a rich premixed zone, -1 a lean premixed zone, and $|0.5|$ a nonpremixed zone for hydrocarbon flames. Since identification of the various reaction zones is more relevant in regions of high reactivity, i.e., where the heat release rates are significant, we have computed ξ_M only in regions where the heat release rate is at least 1% of the maximum heat release rate.

Fig. 5 presents ξ_M contours for propagating CH_4–air flames established with different H_2 enrichment. The contours are shown when the flames are at two different positions, one at $z = 17$ mm corresponding to quasi-steady propagation, and the other near the burner rim ($z \approx 2$) when the flames are in the attachment process at the burner rim. For all four cases considered, the ξ_M contours clearly indicate that during quasi-steady flame propagation, the flames exhibit a triple flame structure at the flame base. The LPZ is weakened with H_2 addition, as indicated by the reduction of the lean premixed wing. For all the four cases, as the flames get close to the burner rim, the LPZ extinguishes and the triple flame transitions to a double flame containing the rich premixed (RPZ) and nonpremixed (NPZ) zones. As these four flames are stabilized at the burner rim, the RPZ gets extinguished due to insufficient mixing near the rim, and the flames exhibit a single (NPZ) flame structure.

In order to further examine the structures of the four flames depicted in Fig. 5 during quasi-steady flame propagation, we present in Fig. 6 the radial profiles of heat release rate and reactant species (CH_4, H_2, and O_2) mass fractions at an axial location $z = 20$ mm near the flame base. The heat release rate profiles have been used in previous investigations [28,49,50] to identify the global flame structure. For all four flames, the heat release rate profiles exhibit three distinct peaks, indicating a triple flame structure. The triple flame structure is also indicated by the CH_4, H_2, and O_2 mass fraction profiles. The effect of H_2 enrichment is to increase the heat release rate in all three reaction zones and to reduce the spatial distance between the nonpremixed and lean premixed reaction zones, and thereby enhance interaction between them.

Since H_2–air premixed flames exhibit wider flammability limits than typical hydrocarbon–air premixed flames, it is relevant to examine the effect of H_2 enrichment on the flammability limits of propagating CH_4–air triple flames. Fig. 7 presents the four flames, discussed in the context of Fig. 5, in terms of the instantaneous heat release rate contours, streamlines,[3] and equivalence ratio contours. The equivalence ratio is computed using $\phi = (f(1 - f_s)/(f_s(1 - f)))$, which implies that the stoichiometric line ($\phi = 1.0$) coincides with the stoichiometric mixture fraction (f_s) line. Previous investigations [47] have used a different equivalence ratio, namely $\phi_u = Y_F/(\nu Y_{ox})$, where ν is the stoichiometric fuel–air mass ratio, based on the reactants' mass fractions in the unburnt mixture. However, the propagating triple flame structure is better characterized using ϕ, since the $\phi_u = 1.0$ line does not coincide with f_s in the burnt region, although it does in the unburnt region. For the 0% H_2-enriched flame, the region of high reactivity (red color) extends from $\phi = 0.46$ to $\phi = 1.58$, which correspond, respectively, to the lean and rich flammability limits of CH_4–air premixed flames [51–53]. There is, however, still significant reactivity beyond these ϕ values, implying that a triple flame extends the flammability limits due to synergistic interactions among the three reaction zones. The H_2 enrichment further extends these flammability limits, since it enhances flame reactivity as well as interactions between the re-

[3] For propagating flames, which represent a dynamic system, streamlines are simply used here to indicate an instantaneous snapshot of the flow field.

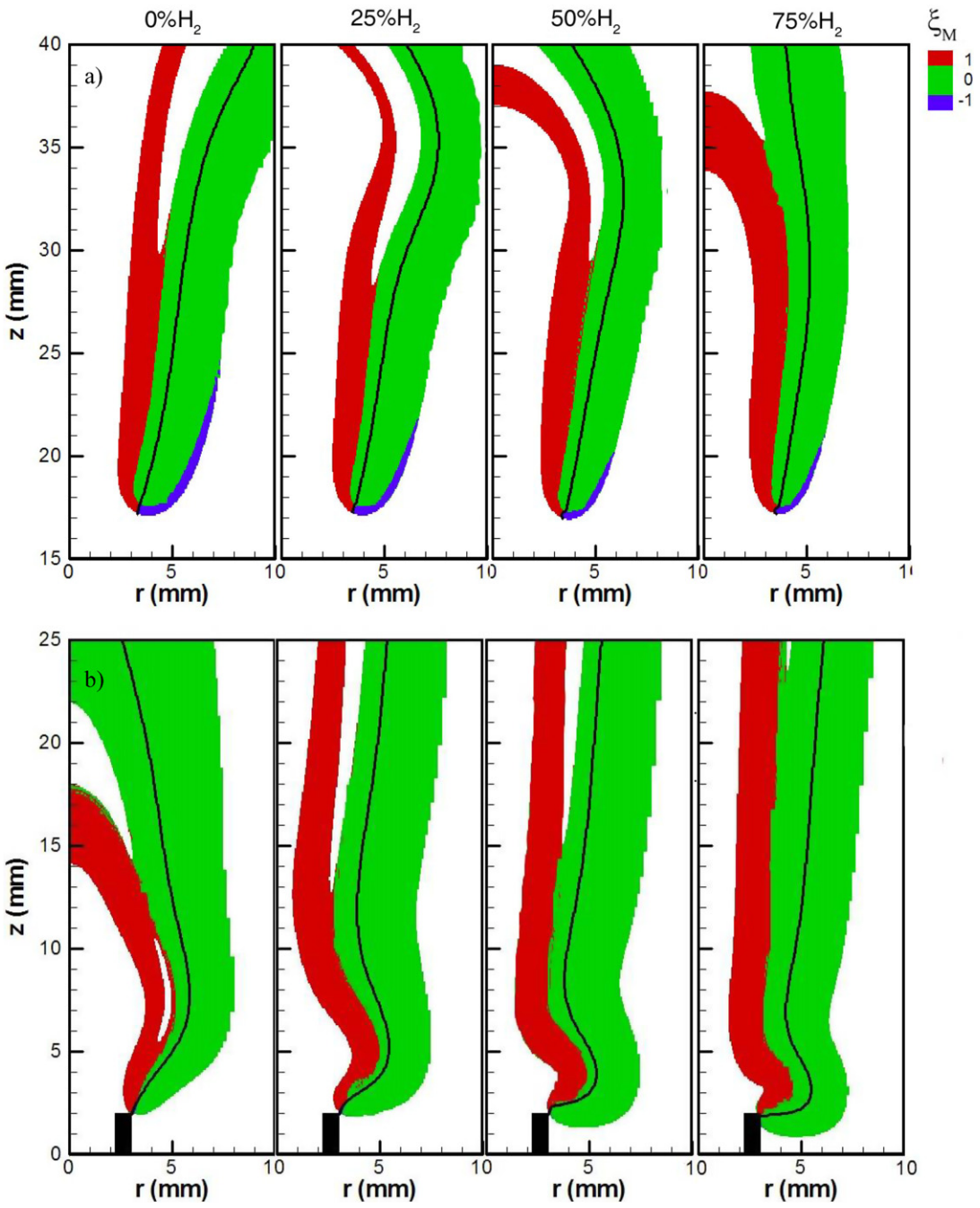

Fig. 5. Flame structures of various H_2-enriched CH_4–air flames are shown through the modified flame index (ξ_M) contours during quasi-steady flame propagation (a) and flame attachment (b).

action zones. For instance, for the 75% H_2-enriched flame, the region of high reactivity (red color) extends from $\phi = 0.14$ to $\phi = 2.54$. H_2 addition also increases both the mixture fraction gradient and the flame curvature, as indicated by the collapsed ϕ lines near the flame base. Moreover, since H_2 enrichment decreases the stoichiometric mixture fraction (f_s), the flame becomes more asymmetric with respect to the $\phi = 1.0$ line. For example, f_s is 0.055 for the 0% H_2-flame, and decreases to 0.044 for the 75% H_2-enriched flame. Consequently, the flow divergence ahead of the flame base becomes more asymmetric with increasing H_2 content. Therefore, the effect of H_2 enrichment is to significantly extend the flamma-

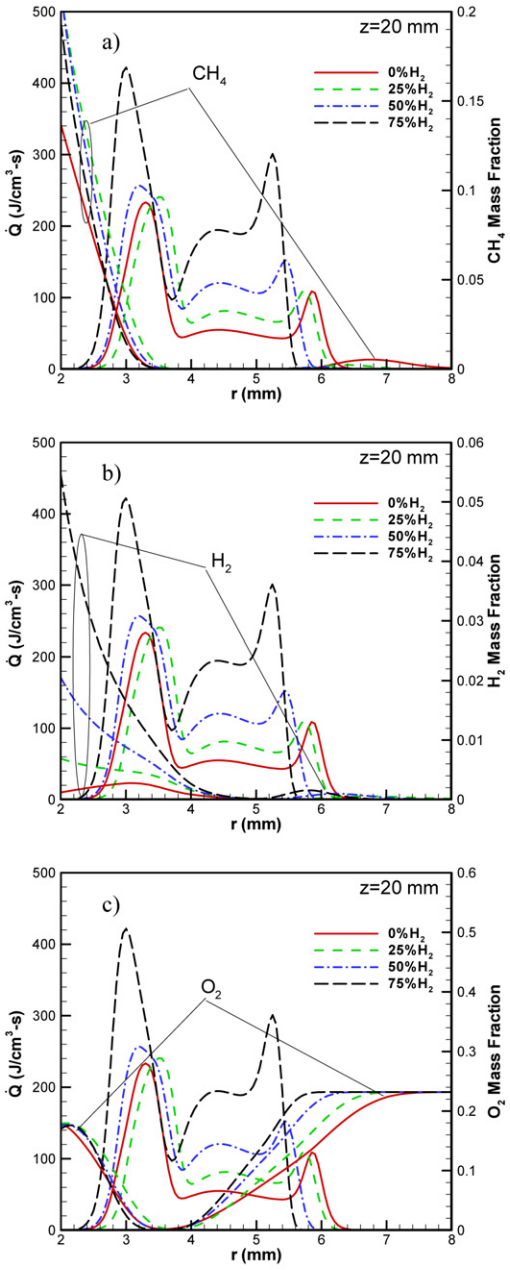

Fig. 6. Flame structure in terms of heat release rate and (a) CH_4, (b) O_2, and (c) H_2 radial profiles as a function of radial distance from the centerline (r) for the 0%, 25%, 50%, and 75% H_2-enriched CH_4–air propagating flames.

bility limits, decrease the radius of curvature at the triple flame base, increase the mixture fraction gradient, and make the flow divergence more asymmetric with respect to the stoichiometric line. These effects influence the flame dynamics, as discussed in the following sections.

Table 1
Lean and rich flammability limits of H_2-enriched CH_4–air planar and triple flames

	Planar flames		Triple flames	
	ϕ_{LEAN}	ϕ_{RICH} [53]	ϕ_{LEAN}	ϕ_{RICH}
0%H_2–100%CH_4	0.46 [51]	1.58	0.30	2.0
25%H_2–75%CH_4	–	1.66	0.20	2.4
50%H_2–50%CH_4	–	1.84	0.14	2.9
75%H_2–25%CH_4	–	2.00	0.10	3.7
100%H_2–0%CH_4	0.14 [52]	2.54	–	–

In order to further quantify the effect of H_2 enrichment on the flammability limits of propagating CH_4–air triple flames, Fig. 8 presents the heat release rate profiles for the four flames as a function of equivalence ratio in the radial direction at an axial location ($z = 20$ mm) near the flame base. As the amount of H_2 in the fuel blend is increased, both the lean and rich flammability limits widen considerably. For instance, the rich flammability limit increases from 2.0 (for the 0% H_2-enriched flame) to 3.7 (for the 75% H_2-enriched flame), while the lean flammability limit increases from 0.3 to 0.1. Table 1 summarizes the lean and rich flammability limits of planar and triple flames.[4] As mentioned before, the triple flame structure exhibits a wider flammability limit than the corresponding planar premixed flames. In addition, the equivalence ratio corresponding to the local maximum heat release rate in the NPZ shifts to the leaner mixture with H_2 enrichment. For instance, these equivalence ratios are $\phi = 0.9$ and 0.8 for the 0% and 75% H_2-enriched flames, respectively. Consequently, the locations of the local maximum heat release rate and the triple point, which is at the stoichiometric line, do not coincide, and the difference becomes more pronounced with the increase in H_2 enrichment. This has implications for accurately determining the flame speed and stretch–flame speed interactions for propagating triple flames.

3.4. Stoichiometric flame structure and preferential diffusion effect

Our simulations indicate that in addition to the enhanced flammability limits, H_2 enrichment also causes a significant increase in the local flame speed of triple flames. Since the flame speed is strongly influenced by preferential mass diffusion effects, we examine in this section the effect of H_2 enrichment on preferential diffusion. The preferential diffusion

[4] The rich and lean flammability limits for each propagating flame are obtained at 2.5% of the maximum heat release rate.

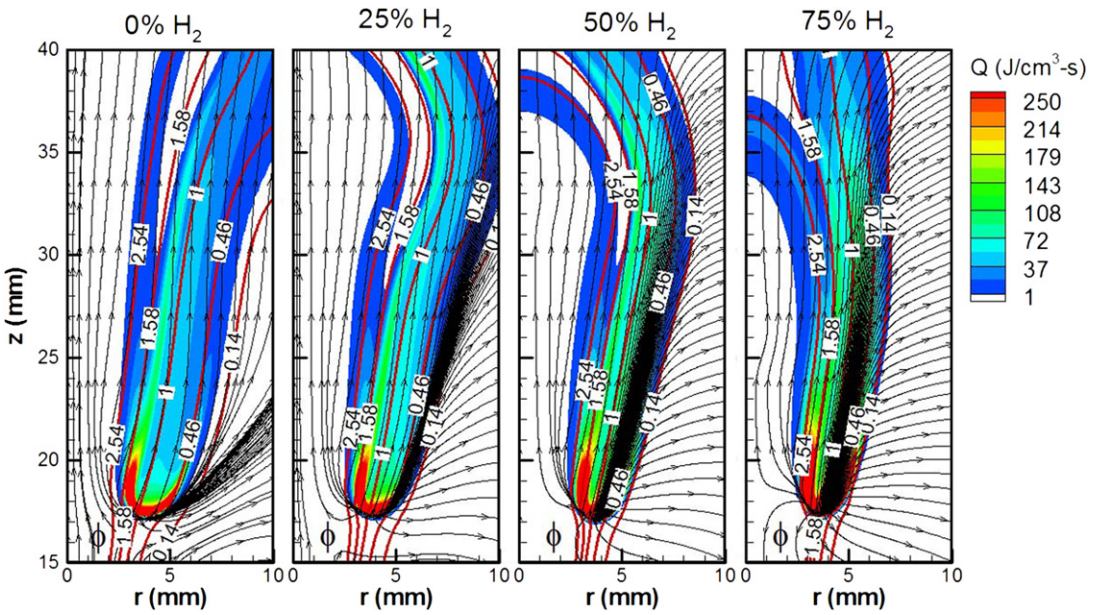

Fig. 7. Computed heat release rate contours (rainbow scheme) (q), equivalence ratio contours (red lines) (ϕ), and flow field streamlines (black lines) (v) for 0%, 25%, 50%, and 75% H_2-enriched CH_4–air propagating flames.

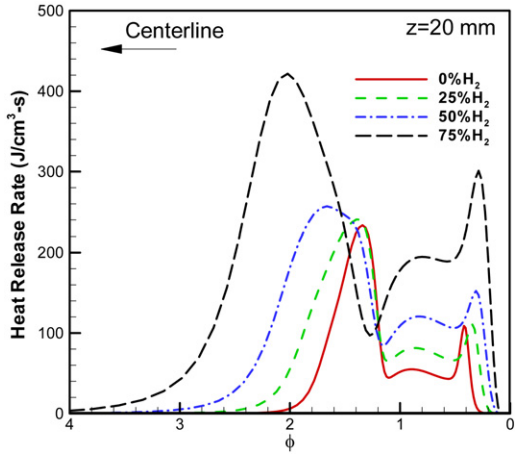

Fig. 8. State relationships in terms of heat release rate radial profiles as a function of equivalence ratio (ϕ) at an axial location of $z = 20$ mm for 0%, 25%, 50%, and 75% H_2-enriched CH_4–air propagating flames in the context of Fig. 7.

effect can be demonstrated by comparing the structure of H_2-enriched propagating triple flames along the stoichiometric mixture fraction with that of the corresponding stoichiometric planar flames.

Lateral diffusion of heat and species plays an important role in determining the structure of propagating triple flames. With fuel blends (say) containing fuels A and B with unequal diffusivities, preferential diffusion of fuel species can lead to localized regions of higher concentration of fuel A compared to fuel B, and this may significantly affect the flame propagation characteristics. This preferential diffusion effect becomes more significant in propagating triple flames that in planar flames due to the presence of lateral diffusion. In order to characterize this effect, we compare the structure of H_2-enriched propagating triple flames along the stoichiometric mixture fraction with that of the corresponding stoichiometric planar flames. Fig. 9 presents these flame structures in terms of the temperature, axial velocity, and major species (CH_4, O_2, H_2O, H_2, CO_2, and CO) profiles for the four H_2-enriched triple flames (discussed in the context of Figs. 7 and 8) and the corresponding stoichiometric planar flames. The two structures are superimposed at the location of the maximum heat release rate. The stoichiometric planar premixed flames were computed using the freely propagating flame simulator of CHEMKIN 4.0 [54] with GRI-Mech 1.2 [41]. The peak flame temperature for triple flames is lower than that for the corresponding planar premixed flames, and this may be attributed to the effects of lateral heat transport and stretch in triple flames. The peak flame temperature, however, increases with H_2 addition for both triple and planar premixed flames.

The presence of preferential diffusion in the case of triple flames can be observed by comparing the CH_4 and H_2 mass fraction profiles for the triple flames and the corresponding planar flames in Fig. 9. For the 0% H_2-enriched case, the CH_4 mass fraction profiles for the triple flame is almost identical to that

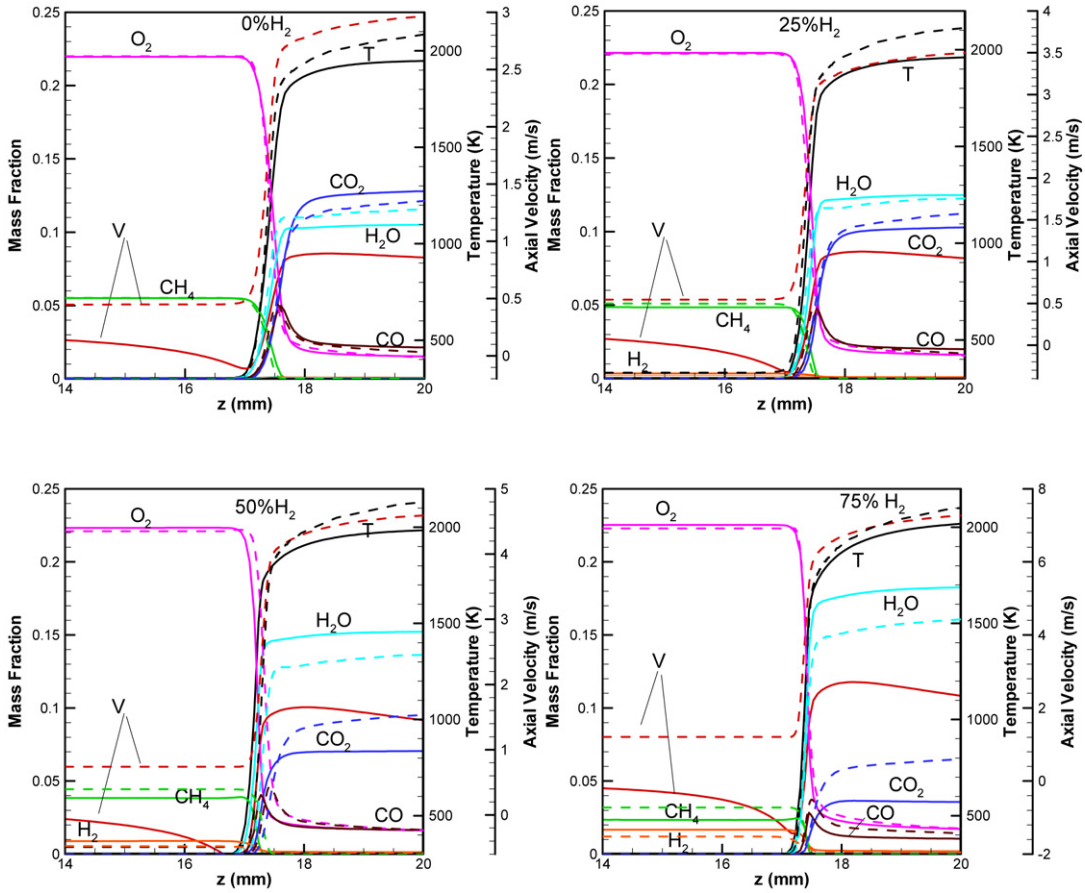

Fig. 9. Comparison of the temperature, axial velocity, and reactants (CH_4, H_2, and O_2) and products (CO_2, CO, and H_2O) mass fraction profiles between the instantaneous flame structure along the stoichiometric mixture fraction line of simulated axisymmetric propagating triple flames (solid) discussed in the context of Fig. 7 and the corresponding stoichiometric planar flames (dashed). The two structures are superimposed at the location of the maximum heat release rate peak.

for the planar premixed flame. However, with increasing H_2 enrichment, the CH_4 mass fraction becomes increasingly smaller while the H_2 mass fraction becomes larger in triple flames than in planar flames, indicating the preferential diffusion of H_2 over CH_4. The reduction in the CH_4 mass fraction due to preferential diffusion is further indicated by the reduced CO and CO_2 mass fractions and the increased H_2O mass fractions for the triple flames compared to those for the planar flames. Therefore, the preferential diffusion of H_2 in H_2-enriched propagating triple flames leads to localized higher concentration of hydrogen, which enhances the local flame speed (S_{tri}).

Another important observation from Fig. 9 is that the axial flow velocity in the case of triple flames reaches a minimum ahead of the flame due to the flow divergence effect. This minimum velocity is associated with the local triple flame speed (S_{tri}). For stationary lifted triple flames, Ruetsch et al. [30] and Im and Chen [33] have shown this minimum velocity to be close to the stoichiometric planar flame speed (S_L). However, for upstream propagating triple flames this minimum velocity becomes negative (cf. Fig. 9) due to flow reversal ahead of the flame. This is consistent with the results reported by Qin et al. [25]. As the amount of H_2 in the fuel blend is increased, the minimum flow velocity increases in magnitude, indicating that the local triple flame speed also increases.

3.5. Flame dynamics at the triple point

In order to examine the flame dynamics and stretch–flame speed interactions, the local flame speed (S_{tri}) and the hydrodynamic (κ_h), curvature-induced (κ_c), and total (κ) stretch rates at the triple point are extracted from our simulations, using the following equations [25,33,55]:

$$S_d^* = \frac{\rho S_d}{\rho_u}, \quad S_d = \left(\frac{1}{\rho |\nabla \varphi|} \left[\nabla \cdot (\rho D \nabla \varphi) + \omega_\varphi \right] \right), \tag{3a}$$

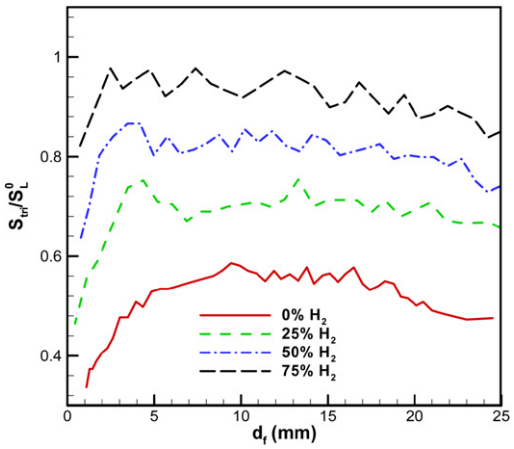

Fig. 10. Normalized local (triple) flame speed (S_{tri}/S_L^0) plotted as a function of distance from the burner rim (d_f) for the 0%, 25%, 50%, and 75% H_2-enriched CH_4–air propagating flames.

$$\kappa_h = \nabla \cdot V_{fluid} - nn : \nabla V_{fluid}, \tag{3b}$$

$$\kappa_c = S_d(\nabla \cdot n), \tag{3c}$$

$$\kappa = \kappa_h + \kappa_c. \tag{3d}$$

In Eq. (3a) the scalar φ is represented by the H_2O mass fraction ($Y_{H_2O} = 0.0727$ [26]). Note that a density-weighted flame speed (S_d^*) is being used, following Im and Chen [33]. Here S_d^* represents the local flame speed along the flame surface, while S_d^* at the triple point yields the local triple flame speed (S_{tri}). In addition, the global flame speed (U_F) is evaluated using [33,56]

$$U_F - U_0 = S_{tri} - U_e = V_f. \tag{4}$$

Here U_0 is the local maximum flow velocity along the stoichiometric mixture fraction line (f_s) ahead of the flame, which is not affected by flow divergence, whereas U_e is the local minimum flow velocity along f_s ahead of the flame. Note that if the flame were to be stabilized as a lifted flame, its displacement flame velocity would be zero ($V_f = 0$), and then $U_F = |U_0|$ and $S_{tri} = |U_e|$.

Fig. 10 presents the normalized local triple flame speed (S_{tri}/S_L^0) as a function of distance from the burner rim (d_f) for the four H_2-enriched CH_4–air triple flames. Here S_L^0 is the stoichiometric unstretched planar flame speed, which is computed for each of the four H_2-enriched flames using the CHEMKIN package [54] with the GRI 1.2 chemistry model [41]. The S_L^0 values for the four flames are provided in Table 2. Several important observations can be made from this figure. First, with increasing H_2 enrichment, S_{tri} increases due to the enhanced chemical reactivity, diffusivity, and preferential diffusion caused by H_2 addition. Second, the ratio S_{tri}/S_L^0 is less than unity, implying that the effect of stretch is to reduce the flame speed for these flames. Third, the difference between S_{tri} and S_L^0 is reduced with increasing H_2 enrichment, implying that the flame becomes less sensitive to stretch rate with H_2 addition. Finally, S_{tri} varies during flame propagation. These aspects are further discussed later in this section.

Table 2
Unstretched flame speeds (S_L^0) and thicknesses (δ_L^0) of H_2-enriched CH_4–air stoichiometric planar premixed flames, computed using the CHEMKIN package [54] and the GRI-Mech. 1.2 [41] chemistry model

	S_L^0 (mm/s)	δ_L^0 (mm)[a]
0%H_2–100%CH_4	400.0	0.47
25%H_2–75%CH_4	497.0	0.44
50%H_2–50%CH_4	693.0	0.37
75%H_2–25%CH_4	1163.0	0.33

[a] Flame thickness was obtained using the gradient method: $\delta_L^0 = (T_{max} - T_{min})/(dT/dx)_{max}$. Here T is the temperature and x is the axial distance in a one-dimensional configuration.

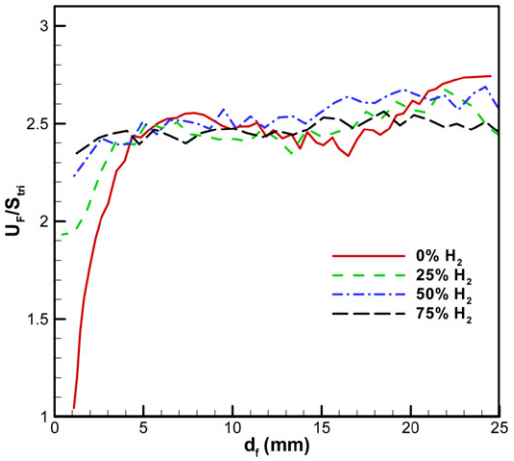

Fig. 11. Normalized global flame speed (U_F/S_{tri}) as a function of distance from the burner rim (d_f) for the 0%, 25%, 50%, and 75% H_2-enriched CH_4–air propagating flames.

Ruetsch et al. [30] and Im and Chen [33] have shown that U_F/S_{tri} is proportional to the square root of the density ratio (i.e., $\sqrt{(\rho_u/\rho_b)}$) in the limit of small mixture fraction gradient. In order to confirm this relationship for our simulations, we present in Fig. 11 the normalized far-field flame speed (U_F/S_{tri}) as a function of flame position (d_f) for the flames discussed in the context of Fig. 10. It is interesting to note that for all H_2-enriched flames, $U_F/S_{tri} \approx 2.5$ during quasi-steady flame propagation. Our simulations also indicate that the square root of the density ratio remains nearly constant ($\sqrt{(\rho_u/\rho_b)} \approx 2.6$) for

all four flames during propagation. While Ruetsch et al. [30] and Im and Chen [33] reported this relationship for triple flames under idealized conditions, our simulations demonstrate a similar relationship under more complex conditions. For instance, Ruetsch et al. [30] used global chemistry with constant thermodynamics and transport properties to establish perfectly symmetric nonbuoyant propagating triple flames in a uniform flow field, while our simulations include detailed chemistry as well as variable transport and thermodynamic properties and show that the flow redirection effect (i.e., $U_F/S_{tri} \approx \sqrt{(\rho_u/\rho_b)}$) is observed for propagating triple flames under more complex conditions, such as nonuniform flow field, presence of buoyancy, flame radiation, and asymmetric flow divergence upstream of the flame.

Fig. 12 presents the hydrodynamic (κ_h), curvature-induced (κ_c), and total (κ) stretch at the triple point plotted as a function of distance from the burner rim (d_f) for the four flames discussed in the context of Fig. 10. As the H_2 enrichment is increased, both κ_h and κ_c and, consequently, the total stretch increase considerably. The increase in κ_h can be attributed to the increased heat release rate at the flame base (cf. Figs. 6, 7, and 8) due to H_2 enrichment, which in turn increases the normal component of flow velocity across the flame front, while the tangential component remains nearly constant. This flow redirection effect, which bends the streamlines toward the stoichiometric mixture fraction line, is responsible for flow divergence ahead of the flame (cf. Fig. 9). The increase in curvature-induced stretch with H_2 enrichment is due to the increase in flame curvature ($\nabla \cdot n$), as discussed in the context of Fig. 7.

It is worth mentioning that the stretch rates for the CH_4–air flame studied here are comparable to those reported by Qin et al. [25] and Ko and Chung [26] for propagating CH_4–air triple flames. For instance, the curvature-induced stretch in the present study is comparable to those reported in the cited studies. While the hydrodynamic stretch (κ_h) is comparable to that reported by Qin et al. [25], it is considerably higher than that reported by Ko and Chung [26]. The difference could be related to the different flow conditions, especially the jet velocity and the absence of coflow in the cited study [26].

In order to examine the stretch–flame speed interactions, we present in Fig. 13 the normalized local triple flame speed (S_{tri}/S_L^0) as a function of the Karlovitz number (Ka) for the flames discussed in the context of Fig. 10. Based on the flame stretch theory, $S_L^0/S_{tri} = 1 + \mathrm{Ma}\,\mathrm{Ka}$ [57], where the Karlovitz number is given by $\mathrm{Ka} = \delta_L^0 \cdot \kappa/S_{tri}$, and the Markstein number (Ma) is equal to the negative of the slope of each curve in this figure. The local triple flame speed decreases almost linearly with increasing Ka

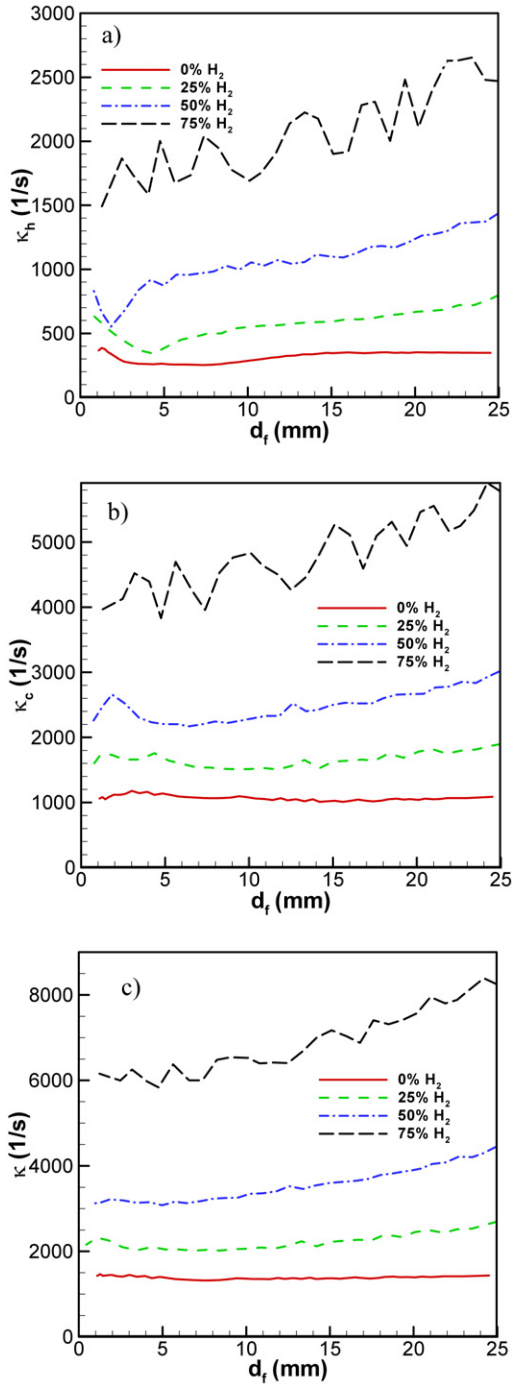

Fig. 12. (a) Hydrodynamic (κ_h), (b) curvature-induced (κ_c), and (c) total (κ) stretch rates at the triple point plotted as a function of distance from the burner rim (d_f) for the propagating 0%, 25%, 50%, and 75% H_2-enriched CH_4–air triple flames.

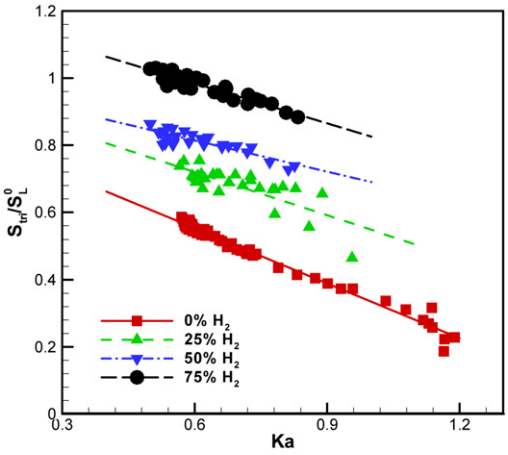

Fig. 13. Normalized local (triple) flame speed (S_{tri}/S_L^0) as a function of Karlovitz number (Ka) for the flames discussed in the context of Fig. 10.

for all cases, implying that these flames are diffusive–thermally stable [57,58]. This result is also consistent with the results reported in Ref. [25] concerning flame speed–stretch interactions in a propagating partially premixed methane–air flame. For a positively stretched flame base, its convex nature toward the fresh mixture defocuses the heat, while focusing the deficient reactant. Thus, for Le $>$ 1.0, the defocusing effect dominates, leading to a negative correlation between local triple flame speed and stretch. In addition, Fig. 13 indicates that the propagating triple flames become less sensitive to stretch (i.e., less diffusive–thermally stable) as H_2 enrichment increases, as indicated by the decrease in the slope (i.e., −Ma). This is consistent with the results shown in Fig. 10. Previous experimental and numerical studies have shown that the flame speed decreases linearly with stretch for stoichiometric outwardly propagating spherical CH_4–air and H_2–air flames (Ka $>$ 0), and that the latter is less sensitive to stretch [57,58]. Therefore, our results are consistent with those reported in the cited studies. Our results are also consistent with the experimental results of Huang et al. [17], who observed that for outwardly propagating spherical flames burning a stoichiometric mixture of natural gas and hydrogen with air, the increase in H_2 content decreases the Markstein number, implying increased tendency toward diffusive–thermal instability.

To characterize the effects of curvature and mixture fraction gradient on triple flame propagation, Fig. 14 presents the normalized local triple flame speed (S_{tri}/S_L^0) as a function of $\delta_L^0 \cdot \nabla \cdot n$ and Da^{-1}, which are, respectively, the dimensionless flame curvature and the dimensionless mixture fraction gradient. Following Ruetsch et al. [30], Da is computed

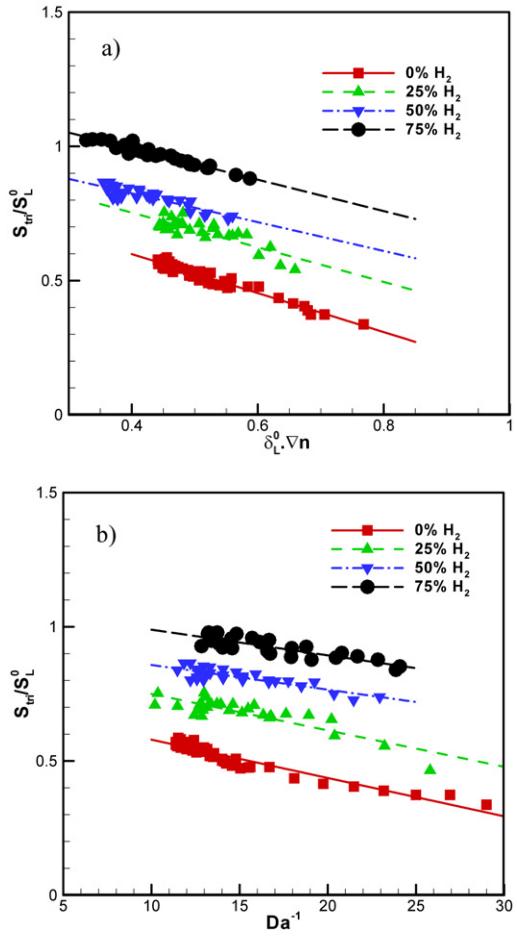

Fig. 14. Normalized local (triple) flame speed (S_{tri}/S_L^0) as a function of (a) dimensionless flame curvature ($\delta_L^0 \cdot \nabla n$) and (b) inverse Damköhler number (Da^{-1}) for the flames discussed in the context of Fig. 10.

at the location of the local minimum flow velocity along f_S. Results indicate a linear correlation between S_{tri}/S_L^0 and $\delta_L^0 \cdot \nabla n$ and between S_{tri}/S_L^0 and Da^{-1} for all the four cases. As $\delta_L^0 \cdot \nabla \cdot n$ increases, S_{tri}/S_L^0 decreases, since the premixed wings are weakened and the propagating triple flame structure resembles more that of a nonpremixed flame. Similarly, with increasing Da^{-1}, S_{tri}/S_L^0 decreases. The response of the local triple flame speed to curvature and mixture fraction gradient is consistent with previous investigations [25,26,30]. Generally, the effect of H_2 enrichment is to reduce the flame's sensitivity to curvature and mixture fraction gradient, as indicated by a decrease in the respective slopes.

Finally, in order to isolate the effect of H_2 enrichment on Markstein numbers (Ma) from that of flame structure, Table 3 summarizes the Markstein numbers for triple flames discussed in the context of Fig. 13

Table 3
Summary of Markstein numbers (Ma) for H_2-enriched CH_4–air planar and triple flames

	Markstein numbers (Ma)	
	Planar flames[a]	Triple flames
0%H_2–100%CH_4	0.42	0.55
25%H_2–75%CH_4	0.26	0.43
50%H_2–50%CH_4	0.19	0.31
75%H_2–25%CH_4	0.11	0.39

[a] Computed under stoichiometric conditions.

and the corresponding counterflow (twin) premixed flames. The Markstein numbers for the latter flames are computed using the CHEMKIN package [54] with the GRI 1.2 chemistry model [41]. The methodology is described in Ref. [59]. An important observation from this table is that triple flames have higher Ma than the corresponding premixed flames, indicating greater sensitivity to stretch and higher diffusive–thermal stability for triple flames.

4. Conclusions

We have presented a numerical investigation on the propagation characteristics of H_2-enriched CH_4–air flames in a nonpremixed jet. Propagating triple flames are established in axisymmetric coflowing jets by igniting the fuel–air mixture at a downstream location. A time-accurate implicit algorithm that uses detailed descriptions of transport and CH_4–air chemistry is used for simulations. The predictions are validated using measurements of the instantaneous displacement flame velocity. The effects of H_2 enrichment on the flame structure, dynamics, and stretch–flame speed interactions for propagating triple flames are characterized.

1. Following ignition, a well-defined triple flame is formed that propagates upstream along the stoichiometric mixture fraction line with a nearly constant displacement flame velocity (V_f). As the flame approaches the burner, it transitions to a double flame and subsequently to a nonpremixed flame, and stabilizes at the burner rim. With increased H_2 concentration in the fuel blend, both V_f and S_{tri} (local triple flame speed) increase progressively due to the enhanced chemical reactivity, diffusivity, and preferential diffusion caused by H_2 enrichment.
2. The propagating triple flame structure is substantially modified by H_2 enrichment, which increases the flame curvature and mixture fraction gradient near the triple point. The addition of H_2 also enhances interactions between the reaction zones, which extend the flammability limits associated with CH_4–air triple flames. In addition, H_2 enrichment makes the flow divergence ahead of the flame more asymmetric with respect to the stoichiometric mixture fraction line. Consequently, the triple point does not coincide with the flame leading edge, which is located at the local minimum flame curvature. This distinction is important in the context of determining S_{tri}, since experimental studies have generally reported flame speeds at the leading edge, while numerical investigations have reported these values at the triple point.
3. The flame dynamics at the triple point is also significantly modified by H_2 enrichment. In addition to the enhancement in local triple flame speed (S_{tri}), H_2 addition considerably increases both the hydrodynamic and curvature-induced stretch, and hence the total stretch. Moreover, the stretch–flame speed interactions are substantially modified, as H_2 enrichment reduces the flame sensitivity to stretch; i.e., it decreases the Markstein number (Ma) and thus increases the flame tendency toward diffusive–thermal instability (i.e., $\mathrm{Ma} \to 0$). These results are consistent with the previously reported experimental results for outwardly propagating premixed spherical flames burning a stoichiometric mixture of natural gas and hydrogen with air.
4. For all the H_2-enriched methane–air flames investigated in this study, the local triple flame speed decreases linearly with stretch. This is consistent with previous studies that have shown a negative correlation between flame speed and stretch for stoichiometric CH_4–air and H_2–air premixed flames with an effective Lewis number greater than one. While S_{tri} decreases linearly with stretch, the ratio U_F/S_{tri} (U_F being the global flame speed) is found to be proportional to the square root of the unburned to burned density ratio ($\sqrt{(\rho_u/\rho_b)}$). This is an important result because it implies that the flame stretch theory and flow redirection effect, which have previously been discussed in the context of idealized flame configurations, also apply to more complex flames such as H_2-enriched CH_4–air triple flames propagating in a nonuniform flow field.
5. Results also indicate that the flammability limits associated with triple flames are significantly wider than those associated with the corresponding planar premixed flames. Triple flames also exhibit higher sensitivity to stretch and greater diffusive–thermal stability than their corresponding stoichiometric planar premixed flames.

References

[1] M.S. Kumar, A. Ramesh, B. Nagalingam, Int. J. Hydrogen Energy 28 (2003) 1143–1154.
[2] F.W. Hoehn, R.L. Baisly, M.W. Dowdy, in: Proc. 10th Intersociety Energy Conversion Conf., Newark, DE, USA, Paper 759173, 1975.
[3] E. Sher, Y. Hacohen, Proc. Inst. Mech. Eng. 203 (1989) 155–162.
[4] V. Raman, J. Hansel, J. Fulton, F. Lynch, D. Bruderly, SAE Publication, 1996, pp. 47–56.
[5] B. Nagalingam, F. Duebel, K. Schmillen, Int. J. Hydrogen Energy 8 (1983) 715–720.
[6] M.R. Swain, M.J. Yusuf, Z. Dulger, M.N. Swain, SAE Paper 932775, 1993.
[7] G.A. Karim, I. Wierzba, Y. Al-Alousi, Int. J. Hydrogen Energy 21 (1996) 625–631.
[8] R.L. Hoekstra, P. Van Blarigan, P.N. Mulligan, SAE Paper 961103.
[9] F. Schafer, SAE Paper 810776, 1996.
[10] C.G. Bauer, T.W. Forest, Int. J. Hydrogen Energy 26 (2001) 71–77.
[11] M.A.S. Al-Baghdadi, Renewable Energy 28 (2002) 1471–1478.
[12] A.R. Choudhuri, S.R. Gollahali, Int. J. Hydrogen Energy 4 (2004) 1293–1302.
[13] G.J. Rortveit, J.E. Hustad, F.A. Williams, in: Proc. 6th Int. Conf. Tech. Combust. Clean Environment, Porto, Portugal, 2000.
[14] S. Naha, S.K. Aggarwal, Combust. Flame 139 (2004) 90–105.
[15] S. Naha, A.M. Briones, S.K. Aggarwal, Combust. Sci. Technol. 177 (2005) 183–220.
[16] C.G. Fotache, T.G. Kreutz, C.K. Law, Combust. Flame 110 (1997) 429–440.
[17] Z. Huang, Y. Zhang, K. Zeng, B. Liu, Q. Wang, D. Jiang, Combust. Flame 146 (2006) 302–311.
[18] C.K. Law, G. Jomass, J.K. Bechtold, Proc. Combust. Inst. 30 (2005) 159–167.
[19] R.W. Schefer, Int. J. Hydrogen Energy 28 (2003) 1131–1141.
[20] E.R. Hawkes, J.H. Chen, Combust. Flame 138 (2004) 242–258.
[21] P.F. Flynn, R.P. Durrett, G.L. Hunter, A.O. Loye, O.C. Akinyemi, J.E. Dec, C.K. Westbrook, SAE Paper 1999-01-0509, 1999.
[22] B.J. Lee, S.H. Chung, Combust. Flame 109 (1997) 163–172.
[23] H. Phillips, Proc. Combust. Inst. 10 (1965) 1277–1283.
[24] P.N. Kioni, B. Rogg, K.N. Bray, A. Liñán, Combust. Flame 95 (1993) 276–290.
[25] X. Qin, C.W. Choi, A. Mukhopadhyay, I.K. Puri, S.K. Aggarwal, V.R. Katta, Combust. Theory Modelling 8 (2004) 293–314.
[26] Y.S. Ko, S.H. Chung, Combust. Flame 118 (1999) 151–163.
[27] J. Lee, S.H. Won, S.H. Jin, S.H. Chung, Combust. Flame 135 (2003) 449–462.
[28] A.J. Lock, A.M. Briones, X. Qin, S.K. Aggarwal, I.K. Puri, U. Hegde, Combust. Flame 143 (2005) 159–173.
[29] A.M. Briones, S.K. Aggarwal, V.R. Katta, Phys. Fluids 18 (2006) 043603.
[30] G.R. Ruetsch, L. Vervisch, A. Liñán, Phys. Fluids 7 (1995) 1447–1454.
[31] R.W. Bilger, Proc. Combust. Inst. 22 (1988) 475–488.
[32] S.F. Ahmed, E. Mastorakos, Combust. Flame 146 (2006) 215–231.
[33] H.G. Im, J.H. Chen, Combust. Flame 119 (1999) 436–454.
[34] I.K. Puri, S.K. Aggarwal, S. Ratti, R. Azzoni, Combust. Flame 124 (2001) 311–325.
[35] S.H. Won, J. Kim, K.J. Hong, M.S. Cha, S.H. Chung, Proc. Combust. Inst. 30 (2005) 339–347.
[36] Z. Shu, S.K. Aggarwal, V.R. Katta, I.K. Puri, Combust. Flame 111 (1997) 276–286.
[37] R. Azzoni, S. Ratti, I.K. Puri, S.K. Aggarwal, Phys. Fluids 11 (1999) 3449–3464.
[38] X. Qin, I.K. Puri, S.K. Aggarwal, V.R. Katta, Phys. Fluids 16 (2004) 2963–2974.
[39] R. Siegel, J.R. Howell, Thermal Radiation Heat Transfer, Hemisphere Publishing Corporation, New York, 1981.
[40] R.C. Reid, J.M. Prausnitz, B.E. Poling, The Properties of Gases and Liquids, McGraw–Hill, New York, 1987.
[41] M. Frenklach, H. Wang, C.-L. Yu, M. Goldenberg, C.T. Bowman, R.K. Hanson, D.F. Davidson, E.J. Chang, G.P. Smith, D.M. Golden, W.C. Gardiner, V. Lissianski, http://www.me.berkeley.edu/gri_mech/; and Gas Research Institute Topical Report: M. Frenklach, H. Wang, M. Goldenberg, G.P. Smith, D.M. Golden, C.T. Bowman, R.K. Hanson, W.C. Gardiner, V. Lissianski, GRI-Mech—An Optimized Detailed Chemical Reaction Mechanism for Methane Combustion, Report No. GRI-95/0058, November 1, 1995.
[42] F.N. Egolfopoulos, D.L. Zhu, C.K. Law, Proc. Combust. Inst. 23 (1990) 471–478.
[43] D.E. Heard, J.B. Jeffries, G.P. Smith, D.R. Crosley, Combust. Flame 88 (1992) 137–148.
[44] V.R. Katta, F. Takahashi, G.T. Linteris, Combust. Flame 137 (2004) 506–522.
[45] V.R. Katta, L.P. Goss, W.M. Roquemore, AIAA J. 32 (1994) 84–94.
[46] Z. Shu, B. Krass, C. Choi, S.K. Aggarwal, V. Katta, I.K. Puri, Proc. Combust. Inst. 27 (1998) 625–632.
[47] X. Qin, Ph.D. thesis, University of Illinois at Chicago, 2004.
[48] H. Yamashita, M. Shimada, T. Takeno, Proc. Combust. Inst. 26 (1996) 27–34.
[49] H. Guo, F. Liu, G.J. Smallwood, Combust. Flame 143 (2005) 282–298.
[50] A.M. Briones, S. Som, S.K. Aggarwal, Combust. Flame 149 (2007) 448–462.
[51] H.C. Barnett, R.R. Hibbard (Eds.), NACA Report 1300, 1959.
[52] M.G. Zabetakis, U.S. Bureau of Mines, Bulletin 627, 1965.
[53] I. Wierzba, B.B. Ale, Int. J. Hydrogen Energy 25 (2000) 75–80.
[54] R.J. Kee, F.M. Rupley, J.A. Miller, M.E. Coltrin, J.F. Grcar, E. Meeks, H.K. Moffat, A.E. Lutz, G. Dixon-Lewis, M.D. Smooke, J. Warnatz, G.H. Evans, R.S. Larson, R.E. Mitchell, L.R. Petzold, W.C. Reynolds, M. Caracotsios, W.E. Stewart, P. Glarborg, C. Wang, C.L. McLellan, O. Adigun, W.G. Houf, C.P. Chou, S.F.

Miller, P. Ho, P.D. Young, D.J. Young, CHEMKIN Release 4.0.2, Reaction Design, San Diego, CA, 2005.
[55] A. Mukhopadyay, I.K. Puri, Combust. Flame 133 (2003) 499–502.
[56] G.R. Ruetsch, J.E. Broadwell, Annual Res. Briefs, Center for Turbulence Research, 1995.
[57] M.I. Hassan, K.T. Aung, G.M. Faeth, Combust. Flame 115 (1998) 539–550.
[58] O.C. Kwon, G.M. Faeth, Combust. Flame 124 (2001) 590–610.
[59] C.K. Wu, C.K. Law, Proc. Combust. Inst. 20 (1985) 1941–1949.